Energy Material Advances
A SCIENCE PARTNER JOURNAL

RESEARCH ARTICLE

Formulating Ether-Based Electrolytes for Highly Reversible Sodium Metal Anodes at High Temperatures

Xiuyun Ren[1], Yanmei Wu[2], Xijie Chen[3], Liang Hu[1], Yu Zhao[1], Tao Zhang[1], Bingcheng Ge[4], Xiaoqi Sun[5*], and Xiaoliang Yu[1*]

[1]Department of Mechanical Engineering and Research Institute for Smart Energy, The Hong Kong Polytechnic University, Hong Kong 999077, China. [2]School of Materials Science and Engineering, Central South University, Changsha 410083, China. [3]College of Chemistry, Nankai University, Tianjin 300071, China. [4]School of Materials Science and Engineering, Henan Normal University, Xinxiang 453007, China. [5]Department of Chemistry, Northeastern University, Shenyang 110819, China.

*Address correspondence to: xiaoliang.yu@polyu.edu.hk (X.Y.); sunxiaoqi@mail.neu.edu.cn (X.S.)

Citation: Ren X, Wu Y, Chen X, Hu L, Zhao Y, Zhang T, Ge B, Sun X, Yu X. Formulating Ether-Based Electrolytes for Highly Reversible Sodium Metal Anodes at High Temperatures. *Energy Mater. Adv.* 2025;6:Article 0184. https://doi.org/10.34133/energymatadv.0184

Submitted 27 October 2024
Revised 19 December 2024
Accepted 20 January 2025
Published 25 April 2025

Battery systems enabling sustainable high energy output at elevated temperatures are highly desirable, especially in high-temperature (HT) environments or hot regions. Sodium metal batteries are attractive next-generation battery technologies with low production costs and high energy densities. The exacerbated detrimental side reactions between the sodium metal anode and the liquid electrolyte at HT, however, reduce sodium plating/stripping reversibility and shorten the cycle life. Ether-based electrolytes are highly compatible with the sodium metal anode, promising good HT electrochemical performances. Nonetheless, the correlation between the molecular structures of ether solvents and HT sodium reversibility has been poorly established because of the complex interfacial reactions. In this study, conventionally used cyclic and linear ethers have been paired with fluorine-rich sodium salt to formulate electrolytes for systematic study. We have revealed that linear ethers outperform cyclic ethers at HT because of their improved thermal stability. Among them, the electrolyte based on diglyme with an appropriate molecular structure delivers the best performance. It strikes a balance in the coordination strength between Na^+ and the solvent, which ensures adequate participation of anions in the solvation sheath while reducing the solvent's electrochemical activity for reductive decomposition at HT. Consequently, it induces the formation of an inorganic-rich solid–electrolyte interphase with compositional uniformity, excellent ionic conductivity, and high mechanical strength. Thus, a high sodium plating/stripping coulombic efficiency of 99.9% has been achieved at a high current density of 5 $mA \cdot cm^{-2}$. As-formulated anode-free sodium metal batteries maintain 80% of the initial capacity after 150 charge/discharge cycles at 60 °C.

Introduction

The growing demand for sustainable battery operation at high temperatures (HTs) is driven by applications in various sectors, including military use, medical devices, and operations in hotter climates and seasons [1–4]. Commercially available lithium-ion batteries (LIBs) face great challenges at HT operation because of accelerated capacity degradation [5,6], the easy generation of lithium dendrites at the graphite anode [7,8], and short-circuit-derived thermal runaway [9–11]. Owing to the remarkable abundance, wide distribution, and economic sustainability of sodium (Na) resources, rechargeable sodium batteries are emerging as compelling alternatives to LIBs for next-generation energy storage systems [12–15]. Importantly, the internal resistance of rechargeable sodium batteries is higher than that of LIBs. When short-circuited, this inherent characteristic of rechargeable sodium batteries limits instantaneous heat generation, resulting in a lower temperature rise and a higher thermal runaway temperature than that of LIBs. Consequently, rechargeable sodium batteries can operate stably even at an HT of 80 °C, exhibiting superior safety [16,17].

Sodium metal batteries (SMBs) stand out among various rechargeable sodium batteries due to the remarkable theoretical specific capacity (1,166 $mAh \cdot g^{-1}$) and low redox potential (−2.71 V vs. standard hydrogen electrode) of sodium metal anodes [18]. Anode-free SMBs pairing a sodium-containing cathode with a bare anode current collector further minimize the anode weight and maximize the energy density of the battery system [19,20]. Despite these advantages, SMBs encounter several crucial challenges that impede their widespread applications [21]. The formation of an unstable solid–electrolyte interphase (SEI) on the sodium anode surface leads to the poor reversibility of sodium plating/stripping, resulting in the deteriorated cycling stability of SMBs, particularly for anode-free SMBs [22,23]. Moreover, the continually growing dendrites during sodium plating/stripping would pierce the separator

and cause a short circuit, resulting in potential safety issues [24–26]. At HT operations, the detrimental interfacial side reactions are exacerbated [27], which further reduces the sodium plating/stripping reversibility and shortens the cycle life of SMBs [27,28].

As the key battery component determining the interfacial reactions, the engineering of electrolytes has been intensively reported to address the challenges for the HT operation of SMBs [27,29,30]. Inspired by previous studies of LIBs, researchers have explored high-boiling-point ester-based electrolytes (e.g., carbonate and phosphate esters) [27,30–32] and high-flash-point solvents like sulfolane [33] and ionic liquids [21] to develop HT electrolytes for SMBs. These electrolytes substantially extended the operational lifespan of SMBs at HT. However, they have poor compatibility with sodium metal anodes, leading to unsatisfactory sodium plating/stripping coulombic efficiency (CE) (data summarized in Table S1). Ether-based electrolytes are emerging as a promising solution for high-performance batteries [34], demonstrating exceptional compatibility with sodium metal anodes and enabling high sodium plating/stripping CE at room temperature [35]. Nonetheless, their applications in HT SMBs have been rarely reported. Recently, 1,2-diethoxyethane was utilized to formulate electrolytes for HT SMBs. The sodium plating/stripping reversibility at HT has yet to be investigated [36]. Dahunsi et al. [22] determined the sodium plating/stripping CE in a commercially available $NaPF_6$–diglyme electrolyte to be 99.3% at 50 °C. Such sodium reversibility is unsatisfactory for the sustainable operation of SMBs, especially for anode-free SMBs. Moreover, the electrochemistry at the sodium anode–ether electrolyte interface remains unexplored. Therefore, there is an urgent need for rational electrolyte formulation toward the sustainable operation of HT SMBs and an in-depth mechanistic understanding of the interfacial reactions.

Herein, this work comprehensively studied the sodium reversibility in various conventionally used linear and cyclic ether-based electrolytes. Linear ethers with better thermal stability have been found to outperform cyclic ethers at HT. Among them, the diglyme-based electrolyte has a balanced coordination strength between Na^+ and the solvent, which ensures adequate participation of anions in the solvation sheath while reducing the solvent's electrochemical activity for reductive decomposition at HT. As a result, it induces the formation of a desirable inorganic-rich SEI. A high sodium plating/stripping CE of 99.9% has been achieved at a high current density of 5 $mA{\cdot}cm^{-2}$, which sustains stable cycling of anode-free SMBs. This work thus provides valuable insights into the interfacial chemistry between the sodium metal anode and electrolytes at HT and will promote the sustainable operation of SMBs at elevated temperatures.

Materials and Methods

Materials

Sodium hexafluorophosphate ($NaPF_6$), 1,2-dimethoxyethane (G1), diethylene glycol dimethyl ether (G2), and tetrahydrofuran (THF) were purchased from DodoChem. Tetraethylene glycol dimethyl ether (G4) and 2-methyltetrahydrofuran (2-MeTHF) were bought from Sigma-Aldrich. The $NaPF_6$ salt was dried overnight at 60 °C using a heating plate. Trace water was removed from all solvents by a pre-treatment with molecular sieves (4 Å). Sodium foils (15.6 mm in diameter) were purchased from Shenzhen Kejing Star Technology Co., Ltd.

Electrode preparation

The cathode active material, sodium vanadium phosphate ($Na_3V_2(PO_4)_3$, NVP), was purchased from Hubei Energy Technology Co., Ltd. and used without any further treatment. The cathode slurry was prepared by mixing the NVP powder, carbon black, and polyvinylidene fluoride (MTI Co., Ltd.) at a mass ratio of 90:5:5 with *N*-methyl-2-pyrrolidinone (Sigma-Aldrich) as the solvent. The mixture was thoroughly stirred to ensure homogeneity. The slurry was uniformly coated onto an aluminum foil current collector with a carbon coating layer (Al/C, MTI Co., Ltd.) using a doctor blade. The coated foil underwent a 2-step drying process: in a blast oven at 110 °C for 12 h, followed by vacuum drying at 100 °C for 12 h. For coin cell assembly, 12-mm-diameter disks were punched from the dried cathode film, and the areal mass loading of NVP was ~5 $mg{\cdot}cm^{-2}$.

Electrochemical tests

Na||Al, Na||NVP, and anode-free Al||NVP batteries were fabricated in CR-2025 coin cells, and Na||Na symmetric batteries were assembled in CR-2032 coin cells. These cells were assembled in an argon-filled glove box (MBRAUN) (O_2 and H_2O < 0.1 ppm). The pre-sodiated NVP cathode was prepared by assembling the Na||NVP cell and then discharging it to 0.1 V versus Na/Na^+ [37]. A separator consisting of a Whatman glass fiber film sandwiched between 2 Celgard 2325 films was utilized in all battery cells. Unless otherwise specified, a 500-μm-thick sodium foil was used as the anode, and the electrolyte volume was controlled to be ~100 μl.

All galvanostatic charge/discharge tests were performed using a LAND CT3001A battery tester. For long-term cycling CE tests, the Na||Al cells were charged-discharged at a low current density of 50 $\mu A{\cdot}cm^{-2}$ for the initial 5 cycles in the voltage range of 0 to 0.5 V versus Na/Na^+ to eliminate surface contamination of the Al foil [38,39]. The average *CE* over the defined cycle range (n) was calculated using the following formula [40]:

$$\text{Average } CE = \frac{1}{n} \times \sum \frac{Q_S}{Q_P} \tag{1}$$

where Q_S and Q_P are the stripped capacity and the plated capacity, respectively. Electrochemical impedance spectroscopy (EIS) measurements were carried out on the cells using an Autolab electrochemical workstation (PGSTAT302N, the Netherlands). The frequency ranges from 100 mHz to 100 kHz with an applied ac amplitude of 5 mV. The ionic conductivities (σ) of electrolytes were measured employing symmetric stainless-steel cells, and they were calculated using the following equation [41]:

$$\sigma = \frac{l}{RA} \tag{2}$$

where R is the ohmic resistance, l is the distance, and A is the area between 2 stainless-steel electrodes, respectively. The Na^+ transference number (t_{Na+}) was measured via the chronoamperometry method and calculated using the following equation [41]:

$$t_{Na+} = \frac{I_{ss}}{I_0} = \frac{I_{ss}(\Delta V - I_0 R_0)}{I_0(\Delta V - I_{ss} R_{ss})} \tag{3}$$

where ΔV is the applied bias voltage, R_0 is the initial impedance, and R_{SS} is the steady-state impedance. The exchange current density (j) was determined from cyclic voltammogram

measurements conducted on Na||Na cells. The values were calculated using the following Tafel equation [42]:

$$\eta = a + b\lg(j) \quad (4)$$

where η is the slope of the Tafel curve and a and b are 2 constants.

Characterization

The electrolyte solvation structure was investigated with a micro-laser confocal Raman spectrometer (Horiba LabRAM HR800, France) using a 532-nm excitation wavelength at room temperature and 60 °C. Morphological observations of sodium deposition on Al current collectors after 40 cycles under 60 °C were realized with a scanning electron microscope (SEM) (Tescan VEGA3). X-ray photoelectron spectroscopy (XPS) was performed utilizing a Thermo Fisher Scientific Nexsa instrument to investigate the chemical composition of the SEI formed in various electrolytes. Atomic force microscope (AFM) morphological characterization was performed using a Bruker Dimension Icon AFM (Bruker, Santa Barbara, CA) located inside an argon-filled glove box. Samples for XPS and AFM analyses were prepared using the Na||Al cells in the plating state.

Theoretical calculations

Molecular dynamics (MD) simulations were performed to elucidate the solvation structure properties of the electrolytes at different temperatures. All MD simulations were conducted using the Forcite module within Materials Studio. A simulation cell was constructed containing randomly distributed sodium salt and solvent molecules, reflecting the experimental electrolyte compositions. The initial cell structure was optimized using the COMPASS II force field. Subsequently, a 3-stage dynamic process was conducted under constant number, pressure, and temperature (NPT) conditions. It comprised a 2.0-ns pre-equilibrium run at 298 K followed by 4-ns equilibrium and production runs at both 298 and 333 K to acquire statistical data [43]. The radial distribution function (RDF) and coordination number (CN) of Na^+ were analyzed using an MD trajectory to understand the solvation shell structure. Additionally, the Na^+ diffusion coefficient was calculated from the mean-squared displacement.

Density functional theory calculations, performed using the Dmol3 module in Materials Studio, provided complementary electronic structure information. The calculations employed the generalized gradient approximations with the Perdew–Burke–Ernzerhof exchange-correlation functions [44]. During geometry optimization, only the ion positions were relaxed until stringent convergence criteria were met (as 3×10^{-4} eV, 0.05 eV·Å^{-1}, and 0.005 Å for energy change, force, and displacement, respectively) [45]. The dielectric constant was adjusted to reflect the specific properties of each solvent.

Results and Discussion

Electrolyte screening for HT SMBs

$NaPF_6$ was selected as the salt, given its moderate lattice energy and fluorine-rich nature [35,46]. To identify suitable electrolytes for stable sodium plating/stripping at elevated temperatures, 1 M $NaPF_6$ was dissolved in various conventionally used cyclic ethers (THF and 2-MeTHF) and linear ether (G1, G2, and G4). The molecular structures of these ethers are shown in Fig. 1A, and the physicochemical properties of these ether solvents are summarized in Table S2. The boiling point is an important indicator describing the thermal stability of solvents, which essentially favors improved electrochemical stability at HT [47]. We can see that the THF, 2-MeTHF, and G1 solvents show relatively lower boiling points below 84 °C. Furthermore, the boiling points increase to 162 °C for G2 and 275 °C for G4. The reversibility of sodium plating/stripping in these electrolytes was evaluated at 60 °C using Na||Al cells. At a current density of 0.5 mA·cm^{-2} and a sodium deposition capacity of 1 mAh·cm^{-2}, the THF, 2-MeTHF, and the G1-based electrolytes exhibited relatively lower initial CE values of 92.7%, 96.7%, and 96.1%, respectively (Fig. 1B). The cycling stability of 2 cyclic ether-based systems was rather poor, with prominent CE fluctuations observed after 50 cycles for THF and only 20 cycles for 2-MeTHF. The G1 system showed stable cycling in the initial cycles, which fluctuated severely afterward. In stark contrast, the G2 and G4 systems demonstrated impressive electrochemical performances, with initial CEs of 97.6% and 97.4%, respectively. Moreover, they showed excellent stability with little CE fluctuation. The average CEs were determined to be as high as 99.6% and 99.4% over 100 cycles, respectively. Such electrochemical performance differences should be ascribed to their distinctions in thermal stability. The THF, 2-MeTHF, and G1 solvents are more conducive to decomposition at the sodium metal surface at HT. They are anticipated to produce organic-rich SEI components, which are unfavorable to sodium plating/stripping stability [48,49].

Given the remarkable performance gap, 1 M $NaPF_6$ G2 and 1 M $NaPF_6$ G4 electrolytes were selected for further study. As the current density increased to 1 mA·cm^{-2}, the cells using the G2 and G4 electrolytes demonstrated stable cycling over 100 cycles, with an average CE of 99.8% (Fig. 1C). The stable polarization voltage and plating/stripping profiles confirmed the excellent electrochemical stability (Fig. 1D and Fig. S1). However, as depicted in Fig. 1E, the CE of the G4 system fluctuated substantially at a current density of 3 mA·cm^{-2}, accompanied by unstable polarization voltages and charge/discharge profiles (Fig. 1F). Moreover, at a current density of 5 mA·cm^{-2}, the G4 system presented poor cycling stability, with CEs of less than 50% and substantial fluctuations in corresponding voltage profiles (Fig. S2). In sharp contrast, the G2 system exhibited stable polarization voltages during sodium plating/stripping (Fig. 1G), maintaining high CEs of 99.8% and 99.9% over 300 cycles at a current density of 3 mA·cm^{-2} (Fig. 1E) and 5 mA·cm^{-2} (Fig. 1H), respectively. The rate-performance difference between the G2 and G4 systems reveals their distinct charge transfer kinetics at the sodium anode–electrolyte interface, which will be further investigated in the following section.

The reversibility of sodium plating/stripping is highly correlated with the uniformity of sodium deposition [35]. Herein, symmetric Na||Na cells were assembled using the G2 and G4 electrolytes and subjected to cycling stability tests at a current density of 1 mA·cm^{-2} and an areal capacity of 1 mAh·cm^{-2} (Fig. S3). For over 500 h of cycling, the G2 electrolyte exhibited superior performance with a lower overpotential of 10 mV, indicating a more uniform sodium deposition [18]. Conversely, the G4 electrolyte showed more than double the overpotential, which gradually increased after 200 h, signifying poorer sodium plating/stripping cyclic stability [21]. SEM observation of Na

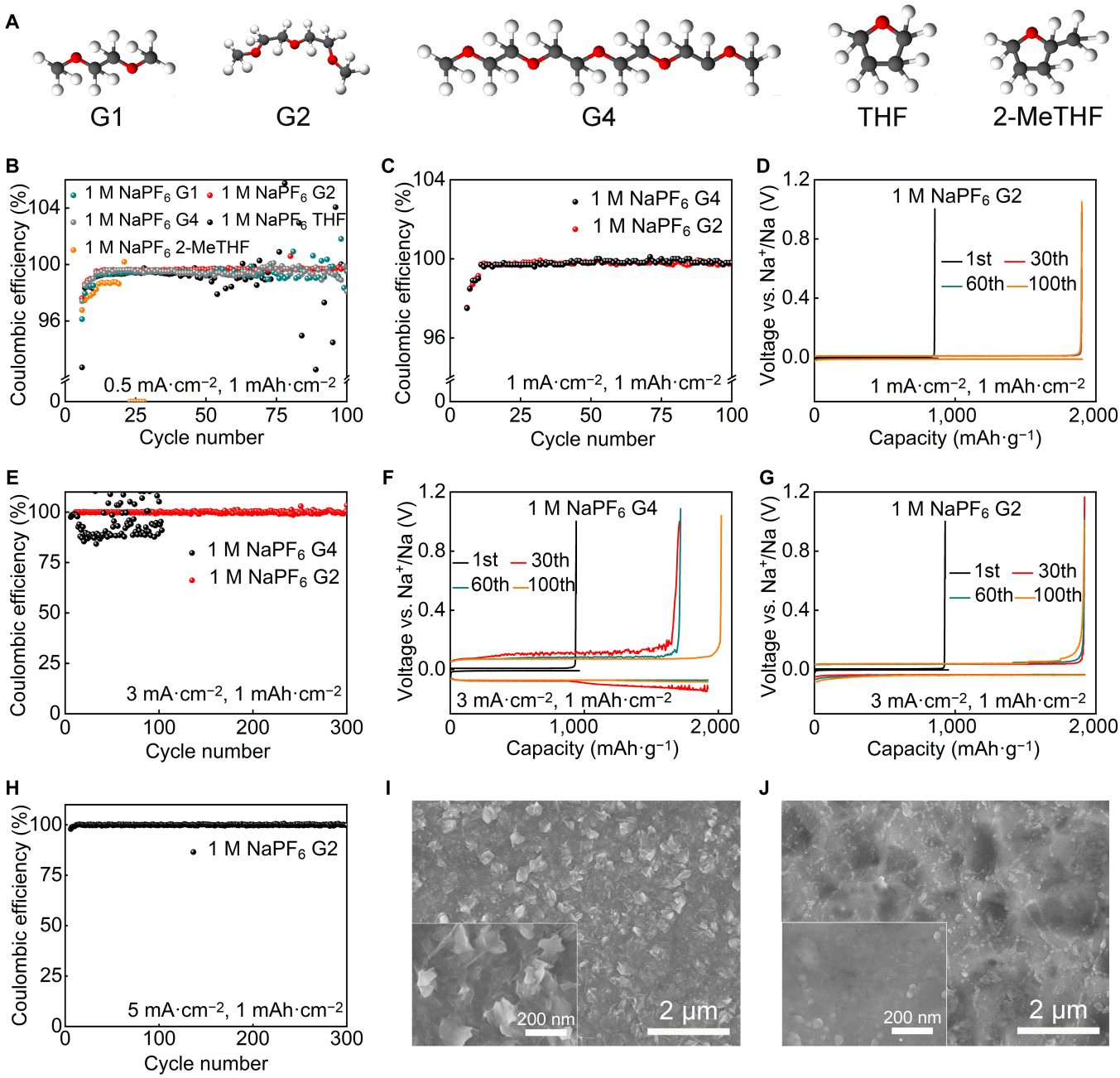

Fig. 1. (A) The molecular structures of the G1, G2, G4, tetrahydrofuran (THF), and 2-methyltetrahydrofuran (2-MeTHF) solvents with C, H, and O atoms drawn in gray, white, and red colors, respectively. (B) Cycling stability of Na||Al cells using different electrolytes at a current density of 0.5 mA·cm^{-2} and a sodium deposition capacity of 1 mAh·cm^{-2} under 60 °C. (C) Cycling stability of G2 and G4 systems at a current density of 1 mA·cm^{-2} and 1 mAh·cm^{-2} under 60 °C. (D) The corresponding voltage profiles of the G2 system at the 1st, 30th, 60th, and 100th plating/stripping cycles at a current density of 1 mA·cm^{-2} and 1 mAh·cm^{-2} under 60 °C. (E) Cycling stability of G2 and G4 systems at a current density of 3 mA·cm^{-2} and 1 mAh·cm^{-2} under 60 °C. The corresponding voltage profiles of G4 (F) and G2 (G) systems at the 1st, 30th, 60th, and 100th plating/stripping cycles at a current density of 3 mA·cm^{-2} and 1 mAh·cm^{-2} under 60 °C. (H) Cycling stability of the G2 system at a current density of 5 mA·cm^{-2} and 1 mAh·cm^{-2} under 60 °C. Scanning electron microscope (SEM) images of the deposited sodium on Al current collectors after 40 cycles of sodium plating/stripping at a current density of 3 mA·cm^{-2}, 1 mAh·cm^{-2} under 60 °C, using the G4 (I) and G2 (J) electrolytes.

plated on Al foil at 60 °C (Fig. 1I and J) further corroborated these findings. In the G4 electrolyte, a rough and irregular surface with a lamellar texture was observed. In contrast, the deposited Na surface was uniform in the G2 electrolyte. This difference in surface morphology could explain the observed disparity in electrochemical performance, highlighting that a uniform sodium deposition surface was more conducive to reversible sodium plating/stripping.

Solvation structure analysis

The solvation structure of Na^+ in electrolytes plays a critical role in determining its migration and desolvation behavior at the electrode/electrolyte interface, ultimately influencing sodium plating/stripping reversibility [50]. Theoretical simulations and experimental methods were combined to elucidate the solvation structures of the G4 and G2 electrolytes. Classical MD simulations were first performed (Fig. 2A and B), with

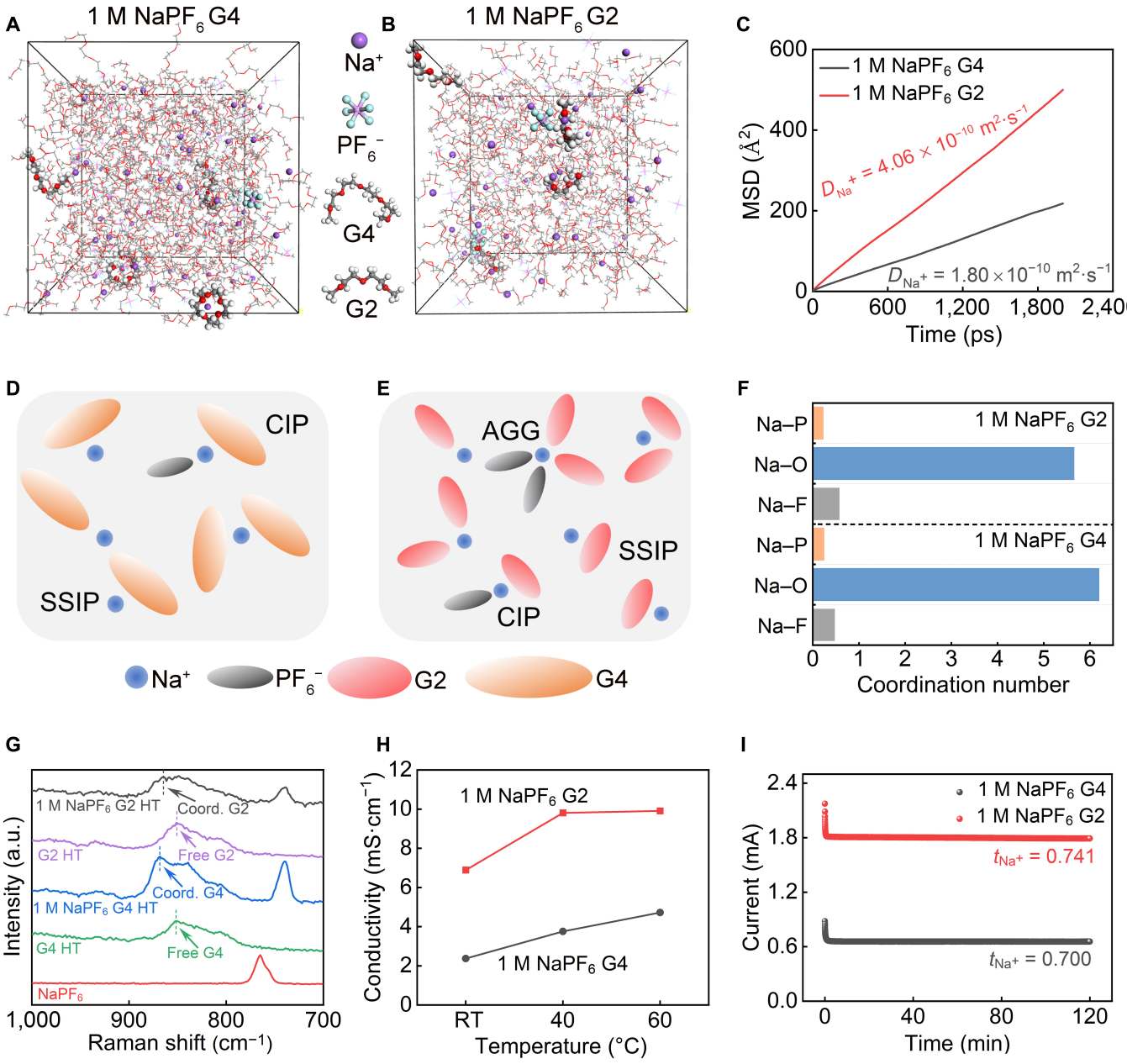

Fig. 2. Snapshots of the G4 (A) and G2 (B) electrolytes at 60 °C obtained from molecular dynamics simulations. (C) Mean-squared displacements of Na^+ in both electrolytes at 60 °C. Schematic illustration of the solvation structure of the G4 (D) and G2 (E) electrolytes. (F) Na^+ coordination numbers with F, O, and P atoms in both electrolytes at 60 °C. (G) Raman spectra of both electrolytes and their components at 60 °C. (H) Temperature-dependent ionic conductivity of both electrolytes. (I) The current response of the Na||Na symmetric cells utilizing both electrolytes under a 10-mV polarization. MSD, mean-squared displacement; SSIP, solvent-separated ion pair; CIP, contact ion pair; AGG, aggregate; RT, room temperature.

representative solvation structures depicted in Fig. 2D and E. In both electrolytes, the dominant solvation structure was the solvent-separated ion pair (SSIP). Analysis of the mean-squared displacement for the first 2 ns of the MD simulation production trajectories (Fig. 2C) revealed a much higher Na^+ diffusion coefficient of the G2 electrolyte (4.06×10^{-10} $m^2 \cdot s^{-1}$) at 60 °C than that of G4 (1.80×10^{-10} $m^2 \cdot s^{-1}$). The RDF and CN were investigated to probe the solvation structures further. The RDF for Na–O (oxygen atoms from the solvent) in both electrolytes exhibited a prominent peak at about 2.3 Å (Fig. S4). The corresponding CN values at 60 °C were calculated to be 5.6 and 6.1 for the G2 and G4 electrolytes, respectively (Fig. 2F). This confirmed that SSIPs were the dominant species in their solvation structures and there are more Na^+ ions coordinated with ether oxygens in the G4 electrolyte. The CN of Na–F and Na–P in the G2 electrolyte increased at HT, indicating a more substantial presence of PF_6^- anions within the solvation sheath compared to that at room temperature (Fig. S5). In contrast, the G4 electrolyte exhibited little change in CN. Quantitative analysis revealed a similar ratio of SSIP to contact ion pair (CIP)/aggregate (AGG) solvates in both electrolytes at 60 °C (Fig. S6E and F). Further investigation into the temperature dependence of solvation structures unveiled distinctions between the G2 and G4 electrolytes (Fig. S6C and

D). The elevated temperature induced greater PF_6^- anions into the G2 solvation structure, resulting in an increased CIP/AGG ratio. This observation suggested a weakened interaction between Na^+ and G2 at higher temperatures [51]. It favors the formation of an inorganic-rich SEI, which is desirable for boosted electrochemical performances. In contrast, the G4 electrolyte exhibited little change in its solvation structure with the elevated temperature.

Raman spectroscopy was employed to experimentally validate the differences in solvation structures between 2 electrolytes. Fig. 2G presents the Raman spectra of 2 electrolytes and their components at 60 °C. A characteristic peak corresponding to the C–O stretching vibration was observed at 851 cm^{-1} in bare pure G2 and G4 solvents [52]. It exhibited blueshifts of 17 and 15 cm^{-1} in the G2 and G4 electrolytes at room temperature, respectively (Fig. S7). Intriguingly, a pronounced blueshift of 18 cm^{-1} in the G4 electrolyte demonstrates a strong interaction between the G4 solvent and Na^+ [45], yet a smaller blueshift of 13 cm^{-1} was observed in the G2 electrolyte, suggesting weaker Na^+–solvent coordination at 60 °C. Furthermore, the higher intensity of this characteristic peak in the G4 electrolyte than in the G2 electrolyte indicates its more robust Na^+–solvent coordination [52]. Additionally, the vibrational spectra of the PF_6^- anion provided further insights into its coordination environment. The stretching vibration of PF_6^-, observed at 764 cm^{-1} in the $NaPF_6$ salt, shifted to approximately 740 cm^{-1} in both electrolytes, which could be attributed to attenuated coordination between PF_6^- and Na^+ after dissociation [53].

Fig. 2H displays the ionic conductivities of the G4 and G2 electrolytes at various temperatures, estimated using symmetric stainless-steel cells based on their impedances (Fig. S8). The G2 electrolyte exhibited ionic conductivities more than twice that of the G4 electrolyte across the tested temperature range. The fast ion migration could facilitate interfacial reaction kinetics and favor enhanced sodium plating/stripping stability. Despite the lower HT ionic conductivity of the G4 electrolyte (4.72 mS·cm^{-1}), it is high enough to sustain smooth battery operation [54]. To evaluate the Na^+ conductivities of both electrolytes, Na^+ transference numbers were determined (Fig. S9). As depicted in Fig. 2I, the t_{Na+} value for the G2 electrolyte was estimated to be as high as 0.741, which favors rapid sodium plating/stripping kinetics.

Mechanistic analysis of high Na reversibility

Forming a stable and robust SEI layer is crucial for ensuring reversible sodium plating/stripping [55]. Frontier molecular orbital theory provides valuable insights into the reactivity and decomposition pathways of electrolyte components. Specifically, a lower lowest unoccupied molecular orbital (LUMO) energy indicates higher susceptibility to reduction, making a molecule more prone to participate in SEI formation reactions on the sodium anode surface [56]. To investigate the formation mechanism of SEI, density functional theory calculations were conducted to obtain the LUMO energy levels of various solvation structures. Fig. 3A and Table S3 summarize the calculated LUMO energy levels of the $NaPF_6$ salt, the G2 and G4 solvents, and the corresponding solvation complexes. As summarized in Table S3, the LUMO energy level of the CIP solvate (Na^+–1G2–$1PF_6^-$, −0.56 eV) in the G2 electrolyte is quite similar to that of the SSIP solvate (Na^+–2G2, −0.64 eV). It predicts the simultaneous reductive decomposition of both solvation complexes. In contrast, the LUMO energy level of the CIP solvate

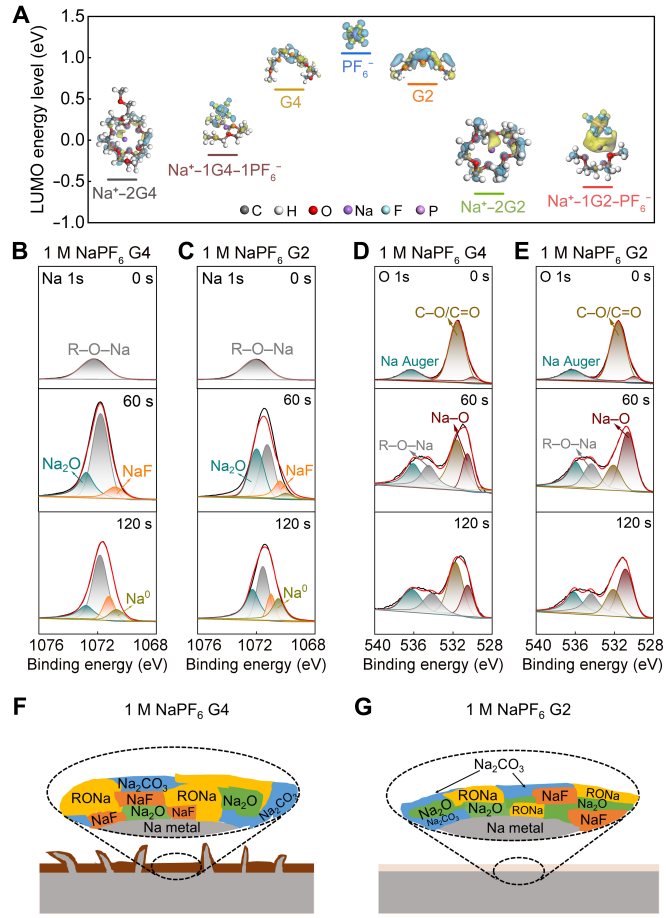

Fig. 3. (A) Lowest unoccupied molecular orbital (LUMO) energy levels of sodium salt, solvent molecules, and solvated complexes in both electrolytes. The in-depth x-ray photoelectron spectroscopy (XPS) Na 1s spectra of the solid–electrolyte interphase (SEI) formed in the G4 (B) and G2 (C) electrolytes at 60 °C. The in-depth XPS O 1s spectra of the SEI formed in the G4 (D) and G2 (E) electrolytes at 60 °C. Schematic illustration of the SEI composition/microstructures in the G4 (F) and G2 (G) electrolytes.

(Na^+–1G4–$1PF_6^-$, −0.17 eV) in the G4 electrolyte is much higher than that of the SSIP solvate (Na^+–2G4, −0.47 eV). It suggests the preferential decomposition of the SSIP solvate and the G4 solvents, which induces the formation of organic-rich SEI. Notably, the LUMO energy level of the CIP solvate (Na^+–1G2–$1PF_6^-$, −0.56 eV) in the G2 electrolyte is much lower than that in the G4 electrolyte (Na^+–1G4–$1PF_6^-$, −0.17 eV), suggesting a greater propensity for decomposition at the sodium anode surface. More importantly, the charge distribution revealed a predominant localization around the PF_6^- anion within the Na^+–1G2–$1PF_6^-$ solvation complex. These analyses collectively indicated that the PF_6^- anion in the G2 electrolyte tends to decompose into favorable inorganic components in the SEI.

To investigate the composition and surface chemistry of the SEI formed in the G4 and G2 electrolytes, depth profile XPS utilizing Ar^+ sputtering was carried out. Fig. 3B to E present the normalized Na 1s and O 1s fine spectra obtained at various sputtering depths. We can see that the SEI formed in the G2 electrolyte displayed mainly inorganic components, i.e., NaF (1,071.4 eV) and Na_2O (1,072.5 eV), in the inner SEI region [35,57]. NaF is deemed a highly desirable SEI component due to its beneficial properties of electronic insulation [58], high

Young's modulus [59], and inherent thermal stability [60]. The SEI formed in the G4 electrolyte, however, exhibited a higher proportion of organic components, primarily characterized by the R–O–Na peak, attributed to the decomposition of the G4 solvent [61].

The O 1s spectra further substantiated the above observations, with a peak at 534.4 eV corresponding to R–O–Na species and a peak at 530.6 eV assigned to Na–O bonds [35]. Intriguingly, a peak corresponding to metallic sodium (Na^0) at 1,071 eV emerged in the G2 electrolyte after 60 s of etching and intensified with increasing sputtering time. This signifies the presence of sodium metal beneath the SEI layer. Notably, the Na^0 peak appeared later in the G4 electrolyte, hinting a potential difference in the SEI thickness. Therefore, the XPS depth profiles revealed a thinner SEI layer formed in the G2 electrolyte than the G4 counterpart, which was further supported by EIS measurements on Na||Na symmetric cells. As shown in Fig. S10, a much lower Na^+ diffusion resistance of 0.03 Ω was determined for the G2 system than the 0.24 Ω for the G4 system, suggesting a thinner SEI formed in G2 [62,63]. It contained a higher concentration of inorganic compounds than the SEI formed in the G4 electrolyte. It suggested a denser and more uniform SEI formed in the G2 electrolyte, favoring rapid and reversible sodium plating/stripping and improved electrochemical stability. Fig. 3F and G illustrate the SEI composition and spatial distribution based on the XPS depth profiling analyses. The G2 system shows a bilayer structure with an inorganic-rich inner layer and an organic-rich outer layer. In contrast, the G4 system demonstrates inorganic species randomly embedded in the organic phase.

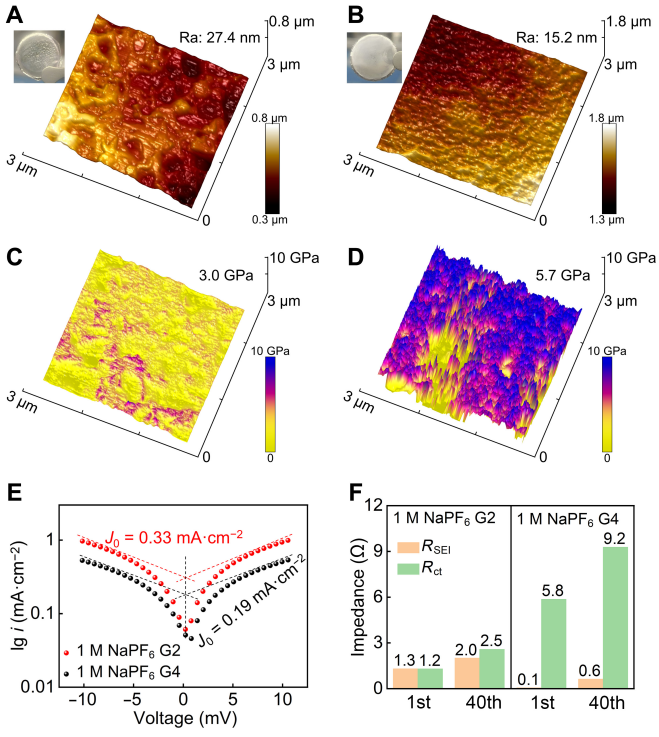

Fig. 4. Atomic force microscope (AFM) surface profiling of the SEI formed in the G4 (A) and G2 (B) electrolytes at 60 °C. Young's modulus mapping of the SEI formed in the G4 (C) and G2 (D) electrolytes at 60 °C. (E) Tafel plots for both electrolytes at 60 °C. (F) The R_{SEI} and R_{ct} values for G4 and G2 electrolytes at 60 °C.

AFM was employed to probe the surface uniformity and mechanical properties of the SEI formed in both electrolytes after 40 cycles at 60 °C. The Al foil surface with plated sodium in the G4 electrolyte presented an uneven morphology with an average roughness of 27.4 nm (Fig. 4A), indicating heterogeneous sodium plating/stripping. In contrast, the topography image of the SEI formed in the G2 electrolyte showed a smoother surface with a much lower average roughness of 15.2 nm (Fig. 4B), proving uniform sodium deposition and reversible sodium stripping. Furthermore, Young's modulus mapping was analyzed to investigate the mechanical properties of the formed SEI. Fig. 4D exhibits that the average Young's modulus of the SEI in the G2 electrolyte was 5.7 GPa, approximately twice that of the SEI formed in the G4 electrolyte (Fig. 4C). This improved mechanical strength might be attributed to inorganic components (NaF and Na_2O) within the SEI, which could effectively withstand dendrite growth and facilitate fast Na^+ transport, thus promoting highly reversible sodium plating/stripping [35,64].

The exchange current density (j_0) was measured to evaluate the intrinsic kinetics of the electron-transfer activity at the interfaces between the sodium anode and electrolytes during sodium plating/stripping at 60 °C [65]. The j_0 values for both electrolytes were determined by linear fitting of Tafel plots (Fig. 4E) obtained from the cyclic voltammogram measurement of Na||Na cells (Fig. S11). j_0 was calculated to be 0.33 mA·cm^{-1} in the G2 electrolyte, much higher than the 0.19 mA·cm^{-1} observed in the G4 electrolyte. This result further supported that a higher concentration of Na^+ beneath the SEI in the G2 electrolyte facilitated uniform sodium deposition. EIS measurements of Na||Al cells were also carried out to assess the interfacial resistance during cycling [35]. The resulting Nyquist plots are depicted in Fig. S12, and quantitative data corresponding to R_{SEI} and the charge transfer process (R_{ct}) are summarized in Fig. 4F. EIS measurements revealed a much smaller R_{ct} in the G2 electrolyte during cycling, while the R_{ct} of the G4 electrolyte increased substantially between the 1st and 40th cycles. This observation verified the faster Na^+ desolvation in the G2 electrolyte, consistent with the results of Na^+ transference number results, resulting in reversible sodium deposition. Therefore, based on combined theoretical and experimental analyses, the desired inorganic-rich SEI formed in the G2 electrolyte, accompanied by its high Na^+ conductivity and Young's modulus, contributed to uniform sodium deposition and reversible stripping.

Electrochemical performance of SMB cells

The rate performance was first investigated by testing Na||NVP cells with the G2 and G4 electrolytes at 60 °C [66]. Cells were cycled at increasing currents from 0.1 to 1.0 A·g^{-1} (Fig. S13). The G2 electrolyte enabled superior rate capability, with the cell retaining 84% of its initial capacity even at a high current density of 1.0 A·g^{-1}. In contrast, the cell with the G4 electrolyte showed much poorer performance, retaining only 76% of its capacity at a mere 0.5 A·g^{-1}. At 1.0 A·g^{-1}, the capacity retention with the G4 electrolyte plummeted to merely 14%.

Inspired by the impressive sodium reversibility and rate performance in the G2 electrolyte, the long-term cycling stability of Na||NVP cells was evaluated. Cells were tested at both room temperature and 60 °C at a current density of 0.5 A·g^{-1}. At room temperature, the cells delivered an initial capacity of 81 mAh·g^{-1} and retained a remarkable 92% of the capacity after 1,000 cycles (Fig. S14). As depicted in Fig. 5A, at an elevated

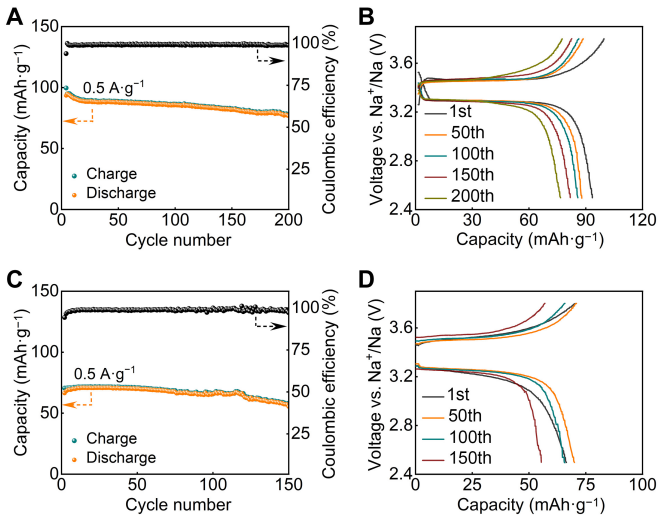

Fig. 5. Long-term galvanostatic cycling performance of Na||$Na_3V_2(PO_4)_3$ (NVP) cells (A) at 0.5 A·g^{-1} under 60 °C and the corresponding galvanostatic charge/discharge curves at the 1st, 50th, 100th, 150th, and 200th cycles (B) using the G2 electrolyte. Long-term galvanostatic cycling performance of anode-free sodium metal batteries (SMBs) (C) at 0.5 A·g^{-1} under 60 °C and the corresponding galvanostatic charge/discharge curves at the 1st, 50th, 100th, and 150th cycles (D) using the G2 electrolyte.

temperature of 60 °C, the cells achieved an even higher initial capacity of 93.5 mAh·g^{-1} and maintained 82% of this capacity after 200 cycles. Impressively, the CE remained stable throughout the cycling, averaging 99.1% over the 200 cycles at 60 °C. The corresponding voltage profiles are illustrated in Fig. 5B. We can observe little depression in the charge/discharge curve, indicating the excellent sodium storage kinetics and stability of the NVP cathode at HT.

To demonstrate the feasibility of the G2 electrolyte for practical applications, anode-free SMBs were assembled using presodiated NVP cathodes (see Materials and Methods for details) and carbon-coated Al current collectors at the anode side. For anode-free cells, excellent long-term cycling stability is demonstrated with an initial capacity of 60 mAh·g^{-1} delivered and 80% of the capacity retained even after 920 cycles at room temperature (Fig. S15). Similarly, the NVP cathode exhibited superior long-cycling stability at 60 °C (Fig. 5C), achieving an initial capacity of 70 mAh·g^{-1} and retaining 80% of this capacity after 150 cycles at 60 °C. As far as we know, such impressive cycling stability of anode-free SMBs at HT operation has been achieved for the first time. It verifies the superiority and practical feasibility of the selected G2 electrolyte for HT SMBs. Fig. 5D illustrates the voltage profiles of the anode-free cells. The charge and discharge voltage plateaus are similar to those of the Na||NVP cells, confirming the rapid kinetics of sodium plating/stripping. Furthermore, there is little depression in the voltage profiles over prolonged cycling, revealing the rapid charge transfer kinetics and stability of the anode-free cells.

Conclusion

In summary, various ether-based electrolytes have been formulated and systematically studied for designing HT electrolytes for high-performance SMBs. Our results have revealed that cyclic ethers are inappropriate for operation at HT because of their poor thermal stability. The diglyme-based electrolyte with a balanced coordination strength between Na^+ and the solvent shows the best performance. Combined theoretical simulations and structural/electrochemical tests demonstrate that it simultaneously allows adequate participation of anions in the solvation sheath and reduced electrochemical activity of the solvent for reductive decomposition at HT. As a result, a favorable inorganic-rich SEI is formed with compositional uniformity, excellent ionic conductivity, and high mechanical strength. A high interfacial exchange current density is realized and an impressive sodium plating/stripping CE of 99.9% is achieved at a high current density of 5 mA·cm^{-2}. The constructed anode-free SMBs maintain 80% of the initial capacity after over 150 charge/discharge cycles at an HT of 60 °C. This work thus provides valuable insights into rational electrolyte formulation for the sustainable operation of SMBs at elevated temperatures.

Acknowledgments

Funding: The authors gratefully acknowledge financial support from the Inner Mongolia Key R&D and Achievement Transformation Plan (No. 2023YFHH0062), the Natural Science Foundation of Guangdong (No. 2023A1515010020), the Young Collaborative Research Grant of the Hong Kong Research Grant Council (C1002-23Y), and the Innovation and Technology Fund (ITS-325-22FP).

Author contributions: X.R.: Writing—original draft, data curation, formal analysis, and investigation. Y.W.: Revision, data curation, and writing—review and editing. X.C.: Writing—review and editing. L.H., Y.Z., T.Z., and B.G.: Data analysis and writing—review and editing. X.S.: Supervision and writing—review and editing. X.Y.: Funding acquisition, conceptualization, supervision, and writing—review and editing.

Competing interests: The authors declare that they have no competing interests.

Data Availability

The authors declare that the data supporting the findings in this study are available within the article and its Supplementary Materials.

Supplementary Materials

Figs. S1 to S15
Tables S1 to S3
Refs. [67–69]

References

1. Geng Z, Lu J, Li Q, Qiu J, Wang Y, Peng J, Huang J, Li W, Yu X, Li H. Lithium metal batteries capable of stable operation at elevated temperature. *Energy Storage Mater*. 2019;23:646–652.
2. Rodrigues M-TF, Babu G, Gullapalli H, Kalaga K, Sayed FN, Kato K, Joyner J, Ajayan PM. A materials perspective on Li-ion batteries at extreme temperatures. *Nat Energy*. 2017;2(8):1–14.
3. Chen Y, Kang Y, Zhao Y, Wang L, Liu J, Li Y, Liang Z, He X, Li X, Tavajohi N, et al. A review of lithium-ion battery safety concerns: The issues, strategies, and testing standards. *J Energy Chem*. 2021;59:83–99.
4. Shen X, Zhang X-Q, Ding F, Huang J-Q, Xu R, Chen X, Yan C, Su F-Y, Chen C-M, Liu X. Advanced electrode materials

in lithium batteries: Retrospect and prospect. *Energy Mater Adv*. 2021;2021:Article 1205324.
5. Peng Y, Zhong C, Ding M, Zhang H, Jin Y, Hu Y, Liao Y, Yang L, Wang S, Yin X, et al. Quantitative analysis of active lithium loss and degradation mechanism in temperature accelerated aging process of lithium-ion batteries. *Adv Funct Mater*. 2024;34(42):Article 2404495.
6. Leng F, Tan CM, Pecht M. Effect of temperature on the aging rate of Li ion battery operating above room temperature. *Sci Rep*. 2015;5(1):Article 12967.
7. Jana A, Woo SI, Vikrant KSN, García RE. Electrochemomechanics of lithium dendrite growth. *Energy Environ Sci*. 2019;12(12):3595–3607.
8. Chen N, Li Y, Dai Y, Qu W, Xing Y, Ye Y, Wen Z, Guo C, Wu F, Chen R. A Li^+ conductive metal organic framework electrolyte boosts the high-temperature performance of dendrite-free lithium batteries. *J Mater Chem A*. 2019;7(16):9530–9536.
9. Feng X, Ren D, He X, Ouyang M. Mitigating thermal runaway of lithium-ion batteries. *Joule*. 2020;4(4):743–770.
10. Hou J, Lu L, Wang L, Ohma A, Ren D, Feng X, Li Y, Li Y, Ootani I, Han X, et al. Thermal runaway of Lithium-ion batteries employing $LiN(SO_2F)_2$-based concentrated electrolytes. *Nat Commun*. 2020;11(1):Article 5100.
11. Guo Q, Xu F, Shen L, Deng S, Wang Z, Li M, Yao X. 20 μm-thick $Li_{6.4}La_3Zr_{1.4}Ta_{0.6}O_{12}$-based flexible solid electrolytes for all-solid-state lithium batteries. *Energy Mater Adv*. 2022;2022:Article 9753506.
12. Li S, Lu X, Li Y, Wang H, Sun Y, Zhou Q, Yue J, Guo R, Wu F, Wu C. Dynamic lock-and-release mechanism enables reduced ΔG at low temperatures for high-performance polyanionic cathode in sodium-ion batteries. *Adv Mater*. 2024;36(49):Article e2413013.
13. Yabuuchi N, Kubota K, Dahbi M, Komaba S. Research development on sodium-ion batteries. *Chem Rev*. 2014;114(23):11636–11682.
14. Liu M, Wu F, Gong Y, Li Y, Li Y, Feng X, Li Q, Wu C, Bai Y. Interfacial-catalysis-enabled layered and inorganic-rich SEI on hard carbon anodes in ester electrolytes for sodium-ion batteries. *Adv Mater*. 2023;35(29):Article 2300002.
15. Chen K, Xia X, Ma H, Xu S, Yao Y, Rui X, Yu Y. Sodiophilic V_2O_3-inducing layer for long lifespan and dendrite-free sodium metal anodes. *Energy Mater Adv*. 2023;4:Article 0063.
16. Zhang F, He B, Xin Y, Zhu T, Zhang Y, Wang S, Li W, Yang Y, Tian H. Emerging chemistry for wide-temperature sodium-ion batteries. *Chem Rev*. 2024;124(8):4778–4821.
17. Che C, Wu F, Li Y, Li Y, Li S, Wu C, Bai Y. Challenges and breakthroughs in enhancing temperature tolerance of sodium-ion batteries. *Adv Mater*. 2024;36(28):Article e2402291.
18. Deng Y, Zheng J, Zhao Q, Yin J, Biswal P, Hibi Y, Jin S, Archer LA. Highly reversible sodium metal battery anodes via alloying heterointerfaces. *Small*. 2022;18(37):Article 2203409.
19. Wu S, Hwang J, Matsumoto K, Hagiwara R. The rational Design of low-barrier fluorinated aluminum substrates for anode-free sodium metal battery. *Adv Energy Mater*. 2023;13(48):Article 2302468.
20. Geng M, Han D, Huang Z, Wang S, Xiao M, Zhang S, Sun L, Huang S, Meng Y. A stable anode-free Na-S full cell at room temperature. *Energy Storage Mater*. 2022;52:230–237.
21. Liu Y, Lu S, Wang Z, Xu J, Weng S, Xue J, Tu H, Zhang F, Liu L, Gao Y. Weakly polar ether-aided ionic liquid electrolyte enables high-performance sodium metal batteries over wide temperature range. *Adv Funct Mater*. 2024;34(28):Article 2312295.
22. Dahunsi OJ, Gao S, Kaelin J, Li B, Razak IBA, An B, Cheng Y. Anode-free Na metal batteries developed by nearly fully reversible Na plating on the Zn surface. *Nanoscale*. 2023;15(7):3255–3262.
23. Zheng X, Li P, Cao Z, Luo W, Sun F, Wang Z, Ding B, Wang G, Huang Y. Boosting the reversibility of sodium metal anode via heteroatom-doped hollow carbon fibers. *Small*. 2019;15(41):Article 1902688.
24. Liu P, Yi H, Zheng S, Li Z, Zhu K, Sun Z, Jin T, Jiao L. Regulating deposition behavior of sodium ions for dendrite-free sodium-metal anode. *Adv Energy Mater*. 2021;11(36):Article 2101976.
25. Sun B, Li P, Zhang J, Wang D, Munroe P, Wang C, Notten PH, Wang G. Dendrite-free sodium-metal anodes for high-energy sodium-metal batteries. *Adv Mater*. 2018;30(29):Article 1801334.
26. Zhang Q, Lu Y, Guo W, Shao Y, Liu L, Lu J, Rong X, Han X, Li H, Chen L, et al. Hunting sodium dendrites in NASICON-based solid-state electrolytes. *Energy Mater Adv*. 2021;2021:Article 9870879.
27. Liu X, Zheng X, Qin X, Deng Y, Dai Y, Zhao T, Wang Z, Yang H, Luo W. Temperature-responsive solid-electrolyte-interphase enabling stable sodium metal batteries in a wide temperature range. *Nano Energy*. 2022;103:Article 107746.
28. Sun Y, Li J-C, Zhou H, Guo S. Wide-temperature-range sodium-metal batteries: From fundamentals and obstacles to optimization. *Energy Environ Sci*. 2023;16(11):4759–4811.
29. Song S, Kotobuki M, Zheng F, Xu C, Savilov SV, Hu N, Lu L, Wang Y, Li WDZ. A hybrid polymer/oxide/ionic-liquid solid electrolyte for Na-metal batteries. *J Mater Chem A*. 2017;5(14):6424–6431.
30. Wang C, Sun Z, Liu Y, Liu L, Yin X, Hou Q, Fan J, Yan J, Yuan R, Zheng M, et al. A weakly coordinating-intervention strategy for modulating Na^+ solvation sheathes and constructing robust interphase in sodium-metal batteries. *Nat Commun*. 2024;15(1):Article 6292.
31. Fu M, Zhang X, Dong W, Li B, Tian R-N, Guo Q, Chen J, Wang D, Dong C, Mao Z. Optimizing Na plating/stripping by a liquid sodiophilic Ga-Sn-In alloy towards dendrite-poor sodium metal anodes. *Energy Storage Mater*. 2023;63:Article 103020.
32. Liu X, Zheng X, Dai Y, Li B, Wen J, Zhao T, Luo W. Suppression of interphase dissolution via solvent molecule tuning for sodium metal batteries. *Adv Mater*. 2023;35(49):Article 2304256.
33. Zheng X, Cao Z, Gu Z, Huang L, Sun Z, Zhao T, Yu S, Wu X-L, Luo W, Huang Y. Toward high temperature sodium metal batteries via regulating the electrolyte/electrode interfacial chemistries. *ACS Energy Lett*. 2022;7(6):2032–2042.
34. Li Y, Wu F, Li Y, Liu M, Feng X, Bai Y, Wu C. Ether-based electrolytes for sodium ion batteries. *Chem Soc Rev*. 2022;51(11):4484–4536.
35. Seh ZW, Sun J, Sun Y, Cui Y. A highly reversible room-temperature sodium metal anode. *ACS Cent Sci*. 2015;1(8):449–455.
36. Zou Y, Zhang B, Luo H, Yu X, Yang M, Zheng Q, Wang J, Jiao C, Chen Y, Zhang H, et al. Electrolyte solvation engineering stabilizing anode-free sodium metal battery with 4.0 V-class layered oxide cathode. *Adv Mater*. 2024;36(47):Article 2410261.

37. Wu J, Lin C, Liang Q, Zhou G, Liu J, Liang G, Wang M, Li B, Hu L, Ciucci F, et al. Sodium-rich NASICON-structured cathodes for boosting the energy density and lifespan of sodium-free-anode sodium metal batteries. *InfoMat*. 2022;4(4):Article e12288.
38. Liu L, Yin YX, Li JY, Wang SH, Guo YG, Wan LJ. Uniform lithium nucleation/growth induced by lightweight nitrogen-doped graphitic carbon foams for high-performance lithium metal anodes. *Adv Mater*. 2018;30(10):Article 1706216.
39. Yu Z, Wang H, Kong X, Huang W, Tsao Y, Mackanic DG, Wang K, Wang X, Huang W, Choudhury S, et al. Molecular design for electrolyte solvents enabling energy-dense and long-cycling lithium metal batteries. *Nat Energy*. 2020;5(7):526–533.
40. Adams BD, Zheng J, Ren X, Xu W, Zhang JG. Accurate determination of coulombic efficiency for lithium metal anodes and lithium metal batteries. *Adv Energy Mater*. 2018;8(7):Article 1702097.
41. Holoubek J, Liu H, Wu Z, Yin Y, Xing X, Cai G, Yu S, Zhou H, Pascal TA, Chen Z, et al. Tailoring electrolyte solvation for Li metal batteries cycled at ultra-low temperature. *Nat Energy*. 2021;6(3):303–313.
42. Xu R, Yan C, Xiao Y, Zhao M, Yuan H, Huang J-Q. The reduction of interfacial transfer barrier of Li ions enabled by inorganics-rich solid-electrolyte interphase. *Energy Storage Mater*. 2020;28:401–406.
43. Efaw CM, Wu Q, Gao N, Zhang Y, Zhu H, Gering K, Hurley MF, Xiong H, Hu E, Cao X, et al. Localized high-concentration electrolytes get more localized through micelle-like structures. *Nat Mater*. 2023;22(12):1531–1539.
44. Zhao Y, Hu Z, Fan C, Liu Z, Zhang R, Han S, Liu J, Liu J. Constructing high-performance N-doped carbon nanotubes anode by tuning interlayer spacing and the compatibility mechanism with ether electrolyte for sodium-ion batteries. *Chem Eng J*. 2022;446(Pt 4):Article 137427.
45. Hu L, Deng J, Lin Y, Liang Q, Ge B, Weng Q, Bai Y, Li Y, Deng Y, Chen G, et al. Restructuring electrolyte solvation by a versatile diluent toward beyond 99.9% Coulombic efficiency of sodium plating/stripping at ultralow temperatures. *Adv Mater*. 2024;36(17):Article 2312161.
46. Ge B, Deng J, Wang Z, Liang Q, Hu L, Ren X, Li R, Lin Y, Li Y, Wang Q. Aggregate-dominated dilute electrolytes with low-temperature-resistant ion-conducting channels for highly reversible Na plating/stripping. *Adv Mater*. 2024;36(41): Article e2408161.
47. Zhang Q-K, Zhang X-Q, Yuan H, Huang J-Q. Thermally stable and nonflammable electrolytes for lithium metal batteries: Progress and perspectives. *Small Sci*. 2021;1(10): Article 2100058.
48. Xue Z, Zhang T, Li X, Wang F, Xu G, Zhu M. Simultaneous regulation of organic and inorganic components in interphase by fiber separator for high-stable sodium metal batteries. *Angew Chem Int Ed Engl*. 2024;64(3):Article e202415283.
49. Wang C, Sun Z, Liu L, Ni H, Hou Q, Fan J, Yuan R, Zheng M, Dong Q. A rooted interphase on sodium via in situ pre-implantation of fluorine atoms for high-performance sodium metal batteries. *Energy Environ Sci*. 2023;16(7):3098–3109.
50. Vineeth S, Soni CB, Sun Y, Kumar V, Seh ZW. Implications of Na-ion solvation on Na anode-electrolyte interphase. *Trends Chem*. 2022;4(1):48–59.
51. Chen T, Jin Z, Liu Y, Zhang X, Wu H, Li M, Feng W, Zhang Q, Wang C. Stable high-temperature lithium-metal batteries enabled by strong multiple ion–dipole interactions. *Angew Chem Int Ed Engl*. 2022;61(35):Article e202207645.
52. Liang HJ, Gu ZY, Zhao XX, Guo JZ, Yang JL, Li WH, Li B, Liu ZM, Li WL, Wu XL. Ether-based electrolyte chemistry towards high-voltage and long-life Na-ion full batteries. *Angew Chem Int Ed Engl*. 2021;60(51):26837–26846.
53. Wu X, Li Z, Feng W, Luo W, Liao L, Cai H, Chen X, Deng Z, Wu J, Xing B, et al. Insights into electrolyte-induced temporal and spatial evolution of an ultrafast-charging Bi-based anode for sodium-ion batteries. *Energy Storage Mater*. 2024;66: Article 103219.
54. Wang Z, Chen C, Wang D, Zhu Y, Zhang B. Stabilizing interfaces in high-temperature NCM811-Li batteries via tuning terminal alkyl chains of ether solvents. *Angew Chem Int Ed Engl*. 2023;135(28):Article e202303950.
55. Liu W, Liu P, Mitlin D. Review of emerging concepts in SEI analysis and artificial SEI membranes for lithium, sodium, and potassium metal battery anodes. *Adv Energy Mater*. 2020;10(43):Article 2002297.
56. Chen X, Hou T-Z, Li B, Yan C, Zhu L, Guan C, Cheng X-B, Peng H-J, Huang J-Q, Zhang Q. Towards stable lithium-sulfur batteries: Mechanistic insights into electrolyte decomposition on lithium metal anode. *Energy Storage Mater*. 2017;8: 194–201.
57. Eshetu GG, Diemant T, Hekmatfar M, Grugeon S, Behm RJ, Laruelle S, Armand M, Passerini S. Impact of the electrolyte salt anion on the solid electrolyte interphase formation in sodium ion batteries. *Nano Energy*. 2019;55:327–340.
58. Ye M, You S, Xiong J, Yang Y, Zhang Y, Li CC. In-situ construction of a NaF-rich cathode-electrolyte interface on Prussian blue toward a 3000-cycle-life sodium-ion battery. *Mater Today Energy*. 2022;23:Article 100898.
59. Zhou X, Liu F, Wang Y, Yao Y, Shao Y, Rui X, Wu F, Yu Y. Heterogeneous interfacial layers derived from the in situ reaction of CoF_2 nanoparticles with sodium metal for dendrite-free Na metal anodes. *Adv Energy Mater*. 2022;12(42):Article 2202323.
60. Sun Y, Shi P, Xiang H, Liang X, Yu Y. High-safety nonaqueous electrolytes and interphases for sodium-ion batteries. *Small*. 2019;15(14):Article 1805479.
61. Tang Z, Wang H, Wu PF, Zhou SY, Huang YC, Zhang R, Sun D, Tang YG, Wang HY. Electrode–electrolyte interfacial chemistry modulation for ultra-high rate sodium-ion batteries. *Angew Chem Int Ed Engl*. 2022;134(18):Article e202200475.
62. Li Q, Ruan J, Weng S, Zhang X, Hu J, Li H, Sun D, Wang X, Fang F, Wang F. Interphasial pre-lithiation and reinforcement of micro-Si anode through fluorine-free electrolytes. *Angew Chem Int Ed Engl*. 2023;62(44):Article e202310297.
63. Koh KH, Lee DJ, Mu A, Kim K, Kim T, Chen Z. Microstructural evolution in lithium plating process and its effect on the calendar storage life. *Nano Res*. 2024;17(10): 8834–8841.
64. Wang X, Lu J, Wu Y, Zheng W, Zhang H, Bai T, Liu H, Li D, Ci L. Building stable anodes for high-rate Na-metal batteries. *Adv Mater*. 2024;36(16):Article 2311256.
65. Anantharaj S, Ede S, Karthick K, Sankar SS, Sangeetha K, Karthik P, Kundu S. Precision and correctness in the evaluation of electrocatalytic water splitting: Revisiting activity parameters with a critical assessment. *Energy Environ Sci*. 2018;11(4):744–771.
66. Chen L, Chen M, Meng Q, Zhang J, Feng G, Ai X, Cao Y, Chen Z. Reconstructing Helmholtz plane enables robust F-rich

Interface for long-life and high-safe sodium-ion batteries. *Angew Chem Int Ed Engl*. 2024;63(38):Article e202407717.
67. Li L, Zhao S, Hu Z, Chou S-L, Chen J. Developing better ester- and ether-based electrolytes for potassium-ion batteries. *Chem Sci*. 2021;12(7):2345–2356.
68. Chen F, Yang Z, Chen Z, Hu J, Chen C, Cai J. Density, viscosity, speed of sound, excess property and bulk modulus of binary mixtures of γ-butyrolactone with acetonitrile, dimethyl carbonate, and tetrahydrofuran at temperatures (293.15 to 333.15) K. *J Mol Liq*. 2015;209:683–692.
69. Jiménez-Gómez CP, García-Sancho C, Cecilia JA, Maireles-Torres P. 2-MeTHF. In: Inamuddin, Boddula R, Asiri AM, editors. *Green sustainable process for chemical and environmental engineering and science: Plant-derived green solvents: Properties and applications*. Amsterdam (the Netherlands): Elsevier; 2021. p. 75–98.